

Relative distance matters for one-shot landmark detection

Qingsong Yao¹, Jianji Wang³, Yihua Sun⁴, Quan Quan¹, Heqin Zhu¹, and S. Kevin Zhou^{1,2}

¹ Key Lab of Intelligent Information Processing of Chinese Academy of Sciences (CAS), Institute of Computing Technology, CAS, Beijing 100190, China

yaoqingsong19@mailsucas.edu.cn

² School of Biomedical Engineering & Suzhou Institute for Advanced Research Center for Medical Imaging, Robotics, and Analytic Computing & LEarning (MIRACLE) University of Science and Technology of China, Suzhou 215123, China

³ Hospital of Guizhou Medical University

⁴ Tsinghua University

Abstract. Contrastive learning based methods such as cascade comparing to detect (CC2D) have shown great potential for one-shot medical landmark detection. However, the important cue of relative distance between landmarks is ignored in CC2D. In this paper, we upgrade CC2D to version II by incorporating a simple-yet-effective relative distance bias in the training stage, which is theoretically proved to encourage the encoder to project the relatively distant landmarks to the embeddings with low similarities. As consequence, CC2Dv2 is less possible to detect a wrong point far from the correct landmark. Furthermore, we present an open-source, landmark-labeled dataset for the measurement of biomechanical parameters of the lower extremity to alleviate the burden of orthopedic surgeons. The effectiveness of CC2Dv2 is evaluated on the public dataset from the ISBI 2015 Grand-Challenge of cephalometric radiographs and our new dataset, which greatly outperforms the state-of-the-art one-shot landmark detection approaches.

Keywords: Medical Landmark Detection · One-shot Learning

1 Introduction

As a fundamental first step in therapy planning and intervention, precise and reliable anatomical landmark detection has attracted great interest from academia and industry [22,15,27,28]. Moreover, it serves as an important step in medical image analysis [14,18], e.g., initialization of segmentation or registration algorithms. Recently, deep learning based methods have great success in efficiently localizing anatomical landmarks in radiological images [2,10,18,15]. Chen et al. [4] regress the heatmap and offset maps simultaneously. Zhong et al. [25] use cascade U-Net to perform a two-stage heatmap regression. Li et al. [12] adapt multiple deep adaptive graphs to capture relationships among landmarks.

A common wisdom is that more training data enhance the supervised methods’ better performance and generalization. However, for medical image analysis, the annotation of datasets needs well-trained, highly-engaged radiologists, which is especially challenging as experts are costly and busy. To break this limitation, an array of self-supervised learning attempts have been explored in classification and segmentation tasks, including image restoration [32,31], patch ordering [34], superpixel-wise [16] and patch-wise [3] contrastive learning [26].

For medical landmark detection, two previous approaches have challenged the hardest scenario: *Only one annotated data is available*. RPR-Net [11] embeds the patches with similar anatomical contexts into close relative positions. Cascade comparing to detect (CC2D) [24] learns to project the pixels with the same anatomical structures into embeddings with high cosine similarities, by solving a self-supervised “patch matching” proxy task in a coarse-to-fine fashion.

Delving into CC2D, despite the great performance with one labeled data available, we find that the important cue of relative distance between landmarks [30,29,5] is ignored. Therefore, we add a novel **relative distance bias (RDB)** in the training stage of CC2D. Theoretical analysis proves that RDB multiplies the gradient of the negative points by a relative distance aware factor, which encourages low similarities for relatively distant points. This add-on term brings two benefits: 1) It makes the framework less possible to detect a wrong point far from the correct landmark; 2) It prevents the encoders from wasting too much effort on decreasing the similarities of the relatively close points with similar anatomical contexts. Here, we name our upgraded version of “relative distance aware cascade comparing to detect” as **CC2Dv2**.

The effectiveness of CC2Dv2 is evaluated by extensive experiments on the public ISBI 2015 Grand-Challenge dataset [8]. Our CC2Dv2 outperforms the state-of-the-art medical one-shot landmark detection methods with a significant accuracy improvement. Furthermore, we contribute an open-source dataset for the measurement of **BioMechanical Parameters of the Lower Extremity (BMPLE)** arising from orthopedic surgery, which is suitable to evaluate the effectiveness of both one-shot and fully-supervised landmark detection methods.

2 Method

The overall framework of CC2Dv2 is build on top of CC2D [24], consisting of two stages: self-supervised learning (SSL) and training from pseudo-labels (TPL). CC2Dv2 differs from CC2D in the SSL stage: *It incorporates a relative distance bias to encourage low similarities between the relatively distant landmarks*. TPL stays the same, that is, using the pseudo-labels generated from SSL stage, a multi-task U-Net [23] is trained to generate heatmap and offset-maps simultaneously, which effectively improves the performance and inference speed [1].

Cascade cosine similarities: The computation flow in CC2Dv2-SSL is the same as in CC2D-SSL [24]. As shown in Fig. 1, let X_r denote an input image resized to $H \times W$, we arbitrarily select a target point $P_r = (x_r, y_r)$. First, we randomly crop a patch X_p containing P_r with size $H_p \times W_p$, and augment the

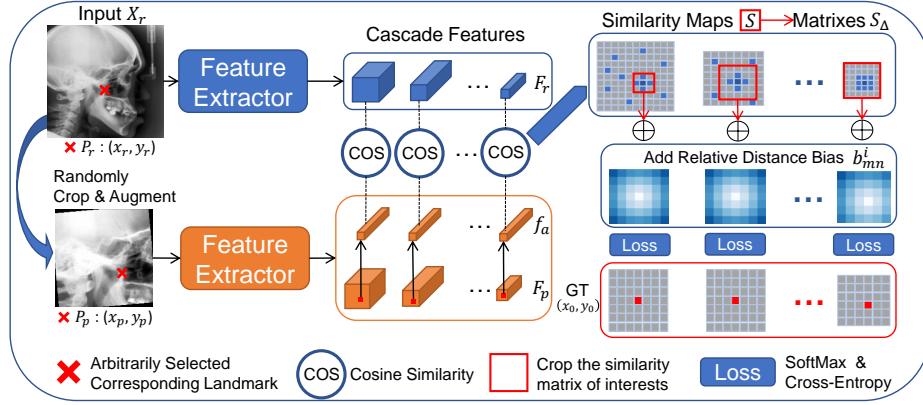


Fig. 1. The training strategy of the proposed relative distance aware cascade comparing (CC2Dv2-SSL). For each layer of the cascade features, CC2Dv2-SSL penalizes the cosine similarities drastically between the selected ground-truth point and the relatively distant points, by adding a novel relative distance bias (RDB) before applying softmax function. As consequence, the feature extractors are encouraged to embed the distant landmarks to the embeddings with low similarities.

content of X_p by rotation and color jittering, which moves the anchor point P_r to $P_p = (x_p, y_p)$. Then, the input X_r and the patch X_p are projected into cascade of multi-scale feature embeddings $F_r = E_r(X_r)$ and $F_p = E_p(X_p)$, by two feature extractors E_r and E_p , respectively. Here, the embedding of i^{th} layer is marked as F^i with size $H_p^i \times W_p^i$. Next, for each layer, we extract the anchor feature f_a^i of the anchor point P_p from F_p^i , guided by its corresponding coordinates $P_a^i = (x_p/2^i, y_p/2^i)$ which are down-sampled for i times. Finally, the cosine similarity map s^i for each layer between input feature F_r^i and anchor feature f_a^i is computed:

$$S^i = \frac{\langle f_a^i \cdot F_r^i \rangle}{\|f_a^i\|_2 \cdot \|F_r^i\|_2}, \quad (1)$$

Then, following CC2D [24], we crop the matrix of interest $S_\Delta^i = \{s_{mn}^i\}_{M \times N}$ from the similarity map $S^i = \{s_{xy}^i\}_{H^i \times W^i}$ with a size of $M \times N$ for each layer. The selected point $P_r^i = (x_r/2^i, y_r/2^i)$ now has a new coordinate $P_t^i = (m_t^i, n_t^i)$ in the matrix S_Δ^i .

Relative distance bias (RDB): Next, we compute the relative Euclidean distance d_{mn}^i for each pixel P_{mn}^i in S_Δ^i with coordinate (m, n) to the selected point $P_t^i = (m_t^i, n_t^i)$ as follow:

$$d_{mn}^i = \sqrt{(m - m_t^i)^2 + (n - n_t^i)^2}, \quad (2)$$

Then the relative distance is clipped to $[0, \beta]$ and added to the cropped cosine similarity matrix S_Δ^i , resulting in relative distance aware similarity matrix W_{mn}^i .

whose element w_{mn}^i is given as:

$$\{w_{mn}^i\}_{M \times N} = \{s_{mn}^i + b_{mn}^i\}_{M \times N}, b_{mn}^i = \{\alpha * clip_{[0,\beta]}(d_{mn}^i)\}_{M \times N}, \quad (3)$$

where α controls the slope of the relative distance.

Cascade comparing to detect: Here, we mark P_t^i as the ground-truth point and denote other non-ground-truth points in matrix W^i (or matrix S_Δ^i) as $P_{\hat{m}\hat{n}}^i$. The ground truth matrix GT^i is computed as $GT_{m_t, n_t}^i = 1, GT_{\hat{m}\hat{n}}^i = 0$. After applying softmax function to normalize W^i to probability matrix Q^i with a temperature τ : $q_{mn}^i = softmax(w_{mn}^i * \tau)$. we use cross-entropy loss L_{CE}^i to increase the probability q_{m_t, n_t}^i of the selected ground-truth point $P_t^i = (m_t^i, n_t^i)$ while decreasing the probabilities $q_{\hat{m}\hat{n}}^i$ of other non-ground-truth points $P_{\hat{m}\hat{n}}^i$ for multi-scale layers:

$$L_{CE}^i(Q^i, GT^i) = - \sum_m \sum_n GT_{mn}^i * \log(q_{mn}^i) = - \log(q_{m_t, n_t}^i), \quad (4)$$

Then, we compute $L_{CE}^i(q^i, GT^i)$ for all layers as final loss L_{SSL} :

$$L_{SSL} = \sum_i L_{CE}^i(Q^i, GT^i), \quad (5)$$

Theoretical analysis: To better understand the effectiveness of the relative distance bias, we compute the partial derivative of L_{CE}^i with respect to the cosine similarities $s_{\hat{m}\hat{n}}^i$ of the negative points $P_{\hat{m}\hat{n}}^i$ in W_Δ^i on the layer i :

$$\begin{aligned} \nabla_{s_{\hat{m}\hat{n}}^i} L_{CE}^i &= \sum_{m,n} \left[\nabla_{q_{mn}^i} L_{CE}^i(q_{mn}^i, GT^i) \times \nabla_{s_{\hat{m}\hat{n}}^i} q_{mn}^i \right] \\ &= - \nabla_{q_{m_t, n_t}^i} \log(q_{m_t, n_t}^i) \times \sum_{m,n} \left(\nabla_{w_{mn}^i} q_{m_t, n_t}^i \times \nabla_{s_{\hat{m}\hat{n}}^i} w_{mn}^i \right) \\ &= - \nabla_{q_{m_t, n_t}^i} \log(q_{m_t, n_t}^i) \times \nabla_{w_{\hat{m}\hat{n}}^i} q_{m_t, n_t}^i \\ &= \frac{\tau * exp(w_{\hat{m}\hat{n}}^i * \tau)}{\sum_{m,n} exp(w_{mn}^i * \tau)} \propto exp(b_{\hat{m}\hat{n}}^i * \tau) * exp(s_{\hat{m}\hat{n}}^i * \tau), \end{aligned} \quad (6)$$

The derivative results show that the relative distance bias d^i directly multiplies the gradient of the cosine similarities $s_{\hat{m}\hat{n}}^i$ of the negative points by $exp(b_{\hat{m}\hat{n}}^i * \tau)$. Accordingly, the negative points farther from the selected GT (positive) point (with greater relative distance $b_{\hat{m}\hat{n}}^i$) are penalized more harshly to have low cosine similarities in the embedding space, *which is exactly what we need*.

Inference steps of SSL stage: Consistent with CC2D [24], the template anchor features f_a are embedded by E_p from the content of the labeled landmark in the template image. Next, we compute cascade cosine similarities s^i between f_a and F_q , where F_q is the query features extracted from the query image by E_r . At last, we multiply the cascade similarities s^i , which are clipped to range $[0, 1]$. The final prediction is returned by *argmax* operator in the coarse-to-fine fashion [24]. We infer the landmark locations for the unlabelled images in the training set as pseudo-labels needed for the TPL stage.

Table 1. Comparison of the state-of-the-art landmark detection methods under fully-supervised and one-shot setting on the cephalometric testset. * represents the performances copied from their original manuscripts, while # represents the performances we re-implement according to the their official code.

Model	Labeled images	MRE (\downarrow) (mm)	SDR (\uparrow) (%)					
			2mm	2.5mm	3mm	4mm	6mm	8mm
Human experts	-	1.07	85.60	90.48	93.64	96.92	99.51	99.83
Ibragimov et al. [7]*	150	-	68.13	74.63	79.77	86.87	-	-
Lindner et al. [13]*	150	1.77	70.65	76.93	82.17	89.85	-	-
Payer et al. [19]*	150	-	73.33	78.76	83.24	89.75	-	-
GU ² -Net[33]#	150	1.69	76.95	83.98	88.82	94.21	98.23	99.14
GU ² -Net[33]#	25	2.41	66.88	76.29	82.40	90.02	95.71	97.45
GU ² -Net[33]#	10	9.79	48.77	58.74	65.07	74.23	80.65	82.61
GU ² -Net[33]#	5	18.88	38.06	46.86	52.91	62.40	70.15	73.52
RPR_Net [11]#	1	4.45	19.45	26.4	36.06	52.74	76.48	88.97
CC2D-SSL [24]*	1	4.67	40.42	47.68	55.54	68.38	-	-
CC2D [24]*	1	2.72	49.81	58.73	68.18	81.01	-	-
CC2Dv2-SSL	1	2.70	44.15	55.16	67.05	81.64	93.87	97.60
CC2Dv2	1	2.23	53.75	64.93	76.48	89.14	97.43	99.16

3 Experiments

3.1 Settings

Dataset: A widely-used public dataset released for cephalometric landmark detection in IEEE ISBI 2015 grand Challenge [21,8] is used, which contains 400 radiographs. 19 landmarks of clinical anatomical significance are labeled by two expert doctors for each radiograph. We take the average annotations as the ground truth. The image size is 1935×2400 and the pixel spacing is 0.1mm. The dataset is split into training and test subsets with 150 and 250 radiographs according to the official website, respectively.

Metrics: Following the challenge [21], we use mean radial error (MRE) and successful detection rate (SDR) as metrics. We set four radii (2mm, 2.5mm, 3mm, and 4mm) for the cephalometric dataset.

Implementation details: The models are implemented in PyTorch [17], accelerated by an NVIDIA TITAN RTX GPU. We resize the images in cephalometric and BMPLE dataset to 384×384 and 384×768 , respectively. For SSL stage, the two feature extractors are optimized by Adam [9] optimizer for 5000 epochs with a learning rate of 0.001 decayed by 0.5 every 500 epochs, with a batch size of 8. The size of cropped patch X_p is set to 192×192 , while the shape of matrix T is 19×19 . The β and α in Eq. 3 are 0.7 and 0.1. For the template image, we choose the 125# training image in cephalometric dataset, and 120# training data in BMPLE dataset. For TPL stage, the multi-task U-Net is optimized by Adam optimizer for 900 epochs with a learning rate of 0.0003 decayed by 0.1 every 300 epochs, with a batch size of 8. We set $\tau = 10$.

3.2 The effectiveness of RDB

We visualize the cosine similarities in Fig. 2(a). Compared with CC2D, the candidate pixels (pixels with similarity $s_{xy}^i > 0$) are more close to the correct

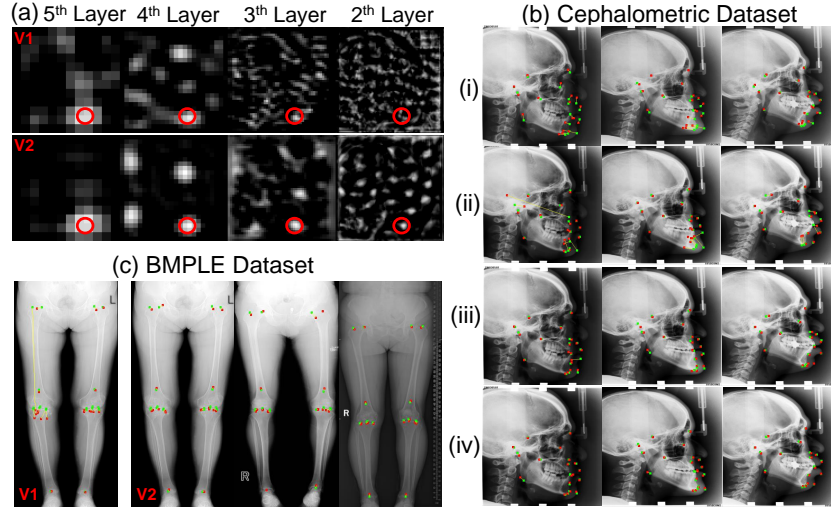


Fig. 2. (a) The comparison between the cosine similarities generated by CC2D and CC2Dv2. The correct landmark is marked in red circle. (b) Visualizations of predictions in cephalometric test dataset. i; ii; iii; iv represent the results inferred from RPR-Net, CC2D-SSL, CC2Dv2-SSL, and CC2D, respectively. The landmarks in green and red are the predictions and ground truths, while the errors are marked in yellow line. (c) Visualizations of testing images in BMPLE dataset predicted by CC2D and CC2Dv2.

landmark, and the cosine similarities are more contrastive, which validate that relative distance bias successfully helps the encoders in CC2Dv2 project the relatively distant landmarks to the embeddings with low similarities. The quantitative performances in Table 1 and the visualizations in Fig. 2(b,c) demonstrate that CC2Dv2 greatly outperforms other one-shot state-of-the-art methods in the two medical landmark detection datasets, and is even competitive to the fully-supervised methods (the first [13] and second [7] place in the ISBI Challenge [21]) in terms of SDR-4mm.

Limitation: Despite that CC2Dv2 effectively decreases MRE by reducing the huge errors (*e.g.*, 4mm SDR for cephalometric dataset is improved from 81.01% to 89.14%), there is still a considerable performance gap compared with fully-supervised methods to precisely detect landmarks with error less than 2mm.

3.3 Hyper-parameter analysis

We study the influence of different settings of the slope α and the maximum value of the RDB β in Eq. 3. According to Table 2, the performances are stable when α lies in $0.7 \sim 1.3$. For β , a small β decreases the effectiveness of RDB. As the maximum value of similarity is 1.0, a too large β makes trouble in the convergence of L_{SSL} . Setting β to 0.7 leads to the best performance.

Table 2. The performances of CC2Dv2-SSL under different settings of the slope α and the maximum value of the RDB β in Eq. 3.

Para.	Value	MRE (\downarrow)		SDR (\uparrow) (%)					
		(mm)		2mm	2.5mm	3mm	4mm	6mm	8mm
β	0.9	2.87	39.12	50.31	62.53	79.39	93.20	96.95	
	0.8	2.82	40.09	51.75	63.6	79.66	93.70	97.35	
	0.7	2.70	44.15	55.16	67.05	81.64	93.87	97.60	
	0.6	2.98	40.55	51.24	62.72	78.38	91.54	95.66	
	0.5	3.14	41.85	51.79	61.98	76.63	89.47	94.42	
α	0.04	3.32	43.32	53.52	63.37	76.57	88.48	93.22	
	0.07	2.73	44.95	55.47	66.67	81.65	93.62	97.01	
	0.10	2.70	44.15	55.16	67.05	81.64	93.87	97.60	
	0.13	2.71	44.86	55.77	67.22	83.01	93.81	97.22	
	0.16	3.07	39.38	50.4	61.47	77.75	91.07	95.34	

Table 3. Comparison of the state-of-the-art landmark detection methods under fully-supervised and one-shot setting on the BMPLE testset.

Model	Labeled images	Test Dataset 1				Test Dataset 2			
		MRE (\downarrow)		SDR (\uparrow) (%)		MRE (\downarrow)		SDR (\uparrow) (%)	
		(mm)		4mm	8mm	12mm	(mm)	4mm	8mm
Human experts	-	1.66	90.50	97.50	98.25	-	-	-	-
Payer et al. [18]	120	5.61	34.00	81.50	95.50	5.92	35.00	78.30	92.60
Chen et al. [4]	120	3.08	85.25	95.25	97.50	3.23	81.80	93.40	96.10
RPR-Net [11]	1	129.2	0.50	1.00	2.00	132.3	0.10	0.10	0.90
CC2D-SSL [24]	1	27.86	17.50	35.00	43.00	30.69	14.60	34.90	45.10
CC2D [24]	1	21.55	14.75	37.25	53.75	20.24	16.50	39.90	56.90
CC2Dv2-SSL	1	12.28	18.25	53.25	77.50	13.60	19.80	46.30	68.90
CC2Dv2	1	7.17	27.25	69.00	88.50	8.18	24.40	62.30	84.40

4 BMPLE Dataset

Clinical significance Biomechanical parameters are essential for orthopedic refined procedures, *e.g.*, measuring the degree of varus/valgus of the knee, planing osteotomy angle, evaluating the improvement of lower limb force lines, and predicting the risk of abnormal wear and loosening of artificial joints [6]. However, BMPLE measurement is time-consuming and laborious for orthopedic surgeons. It takes up to 10 minutes to carefully annotate and connect the bone markers [20].

Data acquisition: The dataset consists of 190 radiographs collected from two collaborated hospitals. The study has been approved by the Hospitals Committee and carried out in accordance with the Declaration of Helsinki. All of the radiographs have been desensitized. The radiographs sizes are distributed from 2396×4950 to 3200×8500 , while the pixel spacing lies in $0.13mm \sim 0.16mm$.

Annotation: The dataset is split into three subsets (Training, Test1, and Test2) with 120, 20, and 50 radiographs, respectively. The radiographs in the training and Test2 subsets are annotated by one senior orthopedic surgeon, while the Test1 subset is labeled by three experts, we compute the average annotations as the ground-truth and report the error of human experts in Table 3.

Measurement of biomechanical parameters of lower extremity relies on accurate anatomical landmark localization. As illustrated in Fig. 3, for each lower limb, 10 landmarks are defined and labeled, 6 axes are generated by connecting

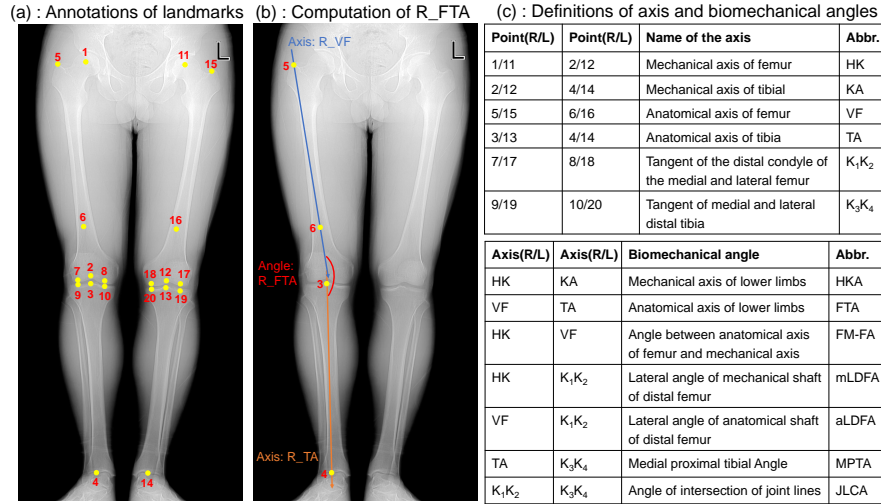


Fig. 3. (a) The illustration of the 20 annotated landmarks in the lower extremity radiography in BMPLE dataset, 1-10 landmarks are on the right (R) lower limb, while the left 11-20 landmarks are on the left (L) lower limb. (b) The biomechanical angle (“Right FTA” in figure b) is calculated between two axes, each axis is connected by two landmarks. (c) The detailed definitions of axis and biomechanical angles.

the corresponding landmarks, and 7 biomechanical angles are computed according to the corresponding two axes [20], the illustrations of other biomechanical angles can be found in the supplemental materials.

Fully supervised performances We establish a preliminary automatic BMPLE measurement framework, which localizes landmarks using the well-trained SOTA method (Chen et al. [4]) and computes BMPLE according the definitions in Fig. 3(b,c). The errors are $3.90^\circ \pm 5.17^\circ$ and $4.25^\circ \pm 7.09^\circ$ on Test1 and Test2 subset, respectively, while the error of human experts on Test1 is $0.69^\circ \pm 2.38^\circ$. The inference speed is 1.55s per image. We hope that this dataset can help the community develop an accurate and fast BMPLE measurement framework, which is valuable to orthopedic surgeons.

One-shot performances Table 3 shows the landmark detection performances of varying competing methods. It is evident that CC2Dv2 clearly outperforms other one-shot approaches by a large margin. However, there is a large performance gap between CC2Dv2 and fully supervised methods and Human experts, which motivates us to improve the accuracy in the future work.

5 Conclusion

In this paper, we upgrade cascade comparing to detect (CC2D) to CC2Dv2, by adding a simple-yet-effective relative distance bias (RDB) in the training stage. The theoretical analysis proves that RDB encourages the encoder to project the

distant landmarks into the embeddings with low cosine similarities. Extensive experiments on two medical landmark detection datasets validate that CC2Dv2 greatly surpasses other state-of-the-art one-shot landmark detection methods. Future work includes developing faster and more accurate methods for the BM-PLE dataset to benefit the orthopedic surgery community.

References

1. Arpit, D., Jastrzebski, S., Ballas, N., Krueger, D., Bengio, E., Kanwal, M.S., Maharaaj, T., Fischer, A., Courville, A., Bengio, Y., et al.: A closer look at memorization in deep networks. In: ICML. pp. 233–242. PMLR (2017)
2. Bhalodia, R., Kavan, L., Whitaker, R.T.: Self-supervised discovery of anatomical shape landmarks. In: MICCAI. pp. 627–638. Springer (2020)
3. Chaitanya, K., Erdil, E., Karani, N., Konukoglu, E.: Contrastive learning of global and local features for medical image segmentation with limited annotations. arXiv preprint arXiv:2006.10511 (2020)
4. Chen, R., Ma, Y., Chen, N., Lee, D., Wang, W.: Cephalometric landmark detection by attentive feature pyramid fusion and regression-voting. In: MICCAI. pp. 873–881. Springer (2019)
5. Criminisi, A., Robertson, D., Konukoglu, E., Shotton, J., Pathak, S., White, S., Siddiqui, K.: Regression forests for efficient anatomy detection and localization in computed tomography scans. *Medical image analysis* **17**(8), 1293–1303 (2013)
6. van Hamersveld, K.T., Marang-van de Mheen, P.J., Nelissen, R.G.: The effect of coronal alignment on tibial component migration following total knee arthroplasty: a cohort study with long-term radiostereometric analysis results. *JBJS* **101**(13), 1203–1212 (2019)
7. Ibragimov, B., Likar, B., Pernus, F., Vrtovec, T.: Computerized cephalometry by game theory with shape-and appearance-based landmark refinement. In: Proceedings of International Symposium on Biomedical imaging (ISBI) (2015)
8. Kaggle: Cephalometric X-Ray Landmarks Detection Challenge (2015), <https://www.kaggle.com/jiahongqian/cephalometric-landmarks/discussion/133268>
9. Kingma, D.P., Ba, J.: Adam: A method for stochastic optimization. ICLR (2015)
10. Lang, Y., Lian, C., Xiao, D., Deng, H., Yuan, P., Gateno, J., Shen, S.G., Alfí, D.M., Yap, P.T., Xia, J.J.: Automatic localization of landmarks in craniomaxillofacial cbct images using a local attention-based graph convolution network. In: MICCAI. pp. 817–826. Springer (2020)
11. Lei, W., Xu, W., Gu, R., Fu, H., Zhang, S., Zhang, S., Wang, G.: Contrastive learning of relative position regression for one-shot object localization in 3d medical images. In: International Conference on Medical Image Computing and Computer-Assisted Intervention. pp. 155–165. Springer (2021)
12. Li, W., Lu, Y., Zheng, K., Liao, H., Lin, C., Luo, J., Cheng, C.T., Xiao, J., Lu, L., Kuo, C.F.: Structured landmark detection via topology-adapting deep graph learning. In: ECCV (2020)
13. Lindner, C., Cootes, T.F.: Fully automatic cephalometric evaluation using random forest regression-voting. *Scientific Reports* **6**, 33581 (2016)
14. Liu, D., Zhou, S.K., Bernhardt, D., Comaniciu, D.: Search strategies for multiple landmark detection by submodular maximization. In: Computer Vision and Pattern Recognition (CVPR), 2010 IEEE Conference on. pp. 2831–2838. IEEE (2010)
15. Liu, W., Wang, Y., Jiang, T., Chi, Y., Zhang, L., Hua, X.S.: Landmarks detection with anatomical constraints for total hip arthroplasty preoperative measurements. In: MICCAI. pp. 670–679. Springer (2020)
16. Ouyang, C., Biffi, C., Chen, C., Kart, T., Qiu, H., Rueckert, D.: Self-supervision with superpixels: Training few-shot medical image segmentation without annotation. In: ECCV. pp. 762–780. Springer (2020)

17. Paszke, A., Gross, S., Massa, F., Lerer, A., Bradbury, J., Chanan, G., Killeen, T., Lin, Z., Gimelshein, N., Antiga, L., et al.: Pytorch: An imperative style, high-performance deep learning library. *Advances in neural information processing systems* **32** (2019)
18. Payer, C., Štern, D., Bischof, H., Urschler, M.: Regressing heatmaps for multiple landmark localization using cnns. In: *MICCAI*. pp. 230–238. Springer (2016)
19. Payer, C., Štern, D., Bischof, H., Urschler, M.: Integrating spatial configuration into heatmap regression based cnns for landmark localization. *Medical image analysis* **54**, 207–219 (2019)
20. Teeter, M.G., Naudie, D.D., McCalden, R.W., Yuan, X., Holdsworth, D.W., MacDonald, S.J., Lanting, B.A.: Varus tibial alignment is associated with greater tibial baseplate migration at 10 years following total knee arthroplasty. *Knee Surgery, Sports Traumatology, Arthroscopy* **26**(6), 1610–1617 (2018)
21. Wang, C.W., Huang, C.T., Lee, J.H., Li, C.H., Chang, S.W., Siao, M.J., Lai, T.M., Ibragimov, B., Vrtovec, T., Ronneberger, O., et al.: A benchmark for comparison of dental radiography analysis algorithms. *Medical Image Analysis* **31**, 63–76 (2016)
22. Yang, D., Xiong, T., Xu, D., Huang, Q., Liu, D., Zhou, S.K., Xu, Z., Park, J., Chen, M., Tran, T.D., et al.: Automatic vertebra labeling in large-scale 3d ct using deep image-to-image network with message passing and sparsity regularization. In: *IPMI*. pp. 633–644 (2017)
23. Yao, Q., He, Z., Han, H., Zhou, S.K.: Miss the point: Targeted adversarial attack on multiple landmark detection. In: *MICCAI*. pp. 692–702. Springer (2020)
24. Yao, Q., Quan, Q., Xiao, L., Kevin Zhou, S.: One-shot medical landmark detection. In: *International Conference on Medical Image Computing and Computer-Assisted Intervention*. pp. 177–188. Springer (2021)
25. Zhong, Z., Li, J., Zhang, Z., Jiao, Z., Gao, X.: An attention-guided deep regression model for landmark detection in cephalograms. In: *MICCAI*. pp. 540–548. Springer (2019)
26. Zhou, H.Y., Yu, S., Bian, C., Hu, Y., Ma, K., Zheng, Y.: Comparing to learn: Surpassing imagenet pretraining on radiographs by comparing image representations. In: *MICCAI*. pp. 398–407. Springer (2020)
27. Zhou, S.K., Greenspan, H., Davatzikos, C., Duncan, J.S., van Ginneken, B., Madabhushi, A., Prince, J.L., Rueckert, D., Summers, R.M.: A review of deep learning in medical imaging: Imaging traits, technology trends, case studies with progress highlights, and future promises. *Proceedings of the IEEE* (2021)
28. Zhou, S.K., Rueckert, D., Fichtinger, G.: *Handbook of Medical Image Computing and Computer Assisted Intervention*. Academic Press (2019)
29. Zhou, S.K.: Shape regression machine and efficient segmentation of left ventricle endocardium from 2d b-mode echocardiogram. *Medical image analysis* **14**(4), 563–581 (2010)
30. Zhou, S.K., Zhou, J., Comaniciu, D.: A boosting regression approach to medical anatomy detection. In: *Computer Vision and Pattern Recognition, 2007. CVPR'07. IEEE Conference on*. pp. 1–8. IEEE (2007)
31. Zhou, Z., Sodha, V., Pang, J., Gotway, M.B., Liang, J.: Models genesis. *Medical image analysis* **67**, 101840 (2021)
32. Zhou, Z., Sodha, V., Siddiquee, M.M.R., Feng, R., Tajbakhsh, N., Gotway, M.B., Liang, J.: Models genesis: Generic autodidactic models for 3d medical image analysis. In: *MICCAI*. pp. 384–393. Springer (2019)
33. Zhu, H., Yao, Q., Xiao, L., Zhou, S.K.: You only learn once: Universal anatomical landmark detection. In: *International Conference on Medical Image Computing and Computer-Assisted Intervention*. pp. 85–95. Springer (2021)

34. Zhu, J., Li, Y., Hu, Y., Ma, K., Zhou, S.K., Zheng, Y.: Rubik's cube+: A self-supervised feature learning framework for 3d medical image analysis. *Medical Image Analysis* **64**, 101746 (2020)